Formation behaviour of blister in cast aluminium alloy

Toda, Hiroyuki
Department of Mechanical Engineering, Kyushu University

Qu, P.C.
Department of Mechanical Engineering, Toyohashi University of Technology

Ito, S.
Department of Mechanical Engineering, Toyohashi University of Technology

Shimizu, K.
Department of Mechanical Engineering, Toyohashi University of Technology

他

出版情報：International Journal of Cast Metals Research. 27 (6), pp.369-377, 2014-06-27.
British Cast Iron Research Association
バージョン：
権利関係：

Formation behaviour of a blister in cast aluminium alloy

H. Toda[a,*], P. C. Qu[b], S. Ito[b], K. Shimizu[b], K. Uesugi[c], A. Takeuchi[c], Y. Suzuki[c] and M. Kobayashi[b]

[a]Department of Mechanical Engineering, Kyushu University, 744, Motooka, Nishi-ward, Fukuoka, FUKUOKA 819-0395, Japan

[b]Department of Mechanical Engineering, Toyohashi University of Technology, 1-1, Hibarigaoka, Tempaku, Toyohashi, Aichi 441-8580, Japan

[c]Japan Synchrotron Radiation Research Institute, 1-1-1, Kouto, Mikazuki-cho, Sayo-gun, Hyogo 679-5198, Japan

Abstract

The formation behaviour of a blister in a die cast aluminium alloy was observed by employing a combined methodology of in-situ 3D observation using X-ray microtomography, and image-based simulation. It has been revealed, via a reverse approach based on the simulation, that nitrogen and carbon dioxide gases fill the blister nucleus. Spontaneous growth of the blister nucleus occurs through creep deformation of the surrounding aluminium, due to the blister nucleus' high internal gas pressure. This internal gas pressure also induces hydrogen precipitation in the form of micro pores, which undergo steady growth in a spherical shell region around the blister nucleus. The selective growth of the micro pores is attributable to the elevation of hydrostatic stress in directions parallel to the casting surface, thereby promoting the expansion of the blister, also parallel to the casting surface, through the absorption of surrounding micro pores into the blister nucleus.

Keywords: Blister, aluminium alloy, micro pore, heat treatment, X-ray tomography, image-based simulation

1. Introduction

A blister is a relatively macroscopic flaw on a metal surface, and typically takes the form of a rounded gas-containing elevation of the surface layer. It has been well documented that the blister formation mechanism is air entrapment during casting [1,2] and/or precipitation of dissolved gas from a solid metal [3-6]. The former has been typically reported in the case of die casting, in which high-speed turbulent fluid is generated in the die casting sleeve, thereby causing gas in the sleeve to become entrapped in the molten metal. It has been reported that in the case of aluminium alloys, nitrogen, carbon dioxide and hydrogen are the major gas species entrapped during die casting [7]. Since blistering usually occurs when die castings are heated to high temperatures, it is impossible to apply a solution heat treatment to die castings to improve their mechanical properties through age-hardening. In addition, with respect to gas precipitation from solids, aluminium and its alloys are highly susceptible to supersaturation with hydrogen, after cooling from a molten to a solidus state, due to the large miscibility gap in hydrogen concentration between molten and solid aluminium [8].

Die castings are produced using high gas pressure intensification, which typically ranges between 70 and 100 MPa. It may seem reasonable to assume that gas entrapped in castings is also pressurized to such a high pressure. This, however, is contradicted by the fact that the pressure level corresponds to a reported yield strength value of 533 K or creep strength value of 478 K [9], and that stress release treatment can usually be applied to die castings at a similar temperature. Difficulties also arise in measuring the gas pressure inside the microscopic nucleus of a blister. It is therefore difficult to assess the actual nucleation and growth process of a blister due to entrapped gas. In terms of gas precipitation, it has been reported that gas pressure is always in thermal equilibrium with the surface tension of a matrix metal, based on the following equation [10]:

$$P = 4\gamma / d \qquad (1)$$

where P is the hydrogen gas pressure, γ is the surface tension of aluminium, and d is the diameter of a pore. A typical blister (5 mm) yields a gas pressure value of about 10^{-3} MPa under the assumption of $\gamma = 1.16$ Nm^{-1}, which is the measured value for the (111) plane [11]. This internal gas pressure would be a few orders of magnitude less than the creep strength level for die cast aluminium alloys at high temperatures [9]. It is therefore impossible to account for such blistering solely in terms of the presence of supersaturated hydrogen.

The objective of the present study is to investigate the nucleation and growth mechanisms of a cast aluminium alloy blister during high temperature exposure, using state-of-the-art synchrotron X-ray microtomography. Neither imaging nor measurement techniques do not provide direct gas pressure data for the nucleus of a blister. A reverse approach was therefore applied to estimate the pressure based on a combined methodology of in-situ three-dimensional (3D) observation and 3D image-based numerical simulation.

2. Experimental and numerical simulation procedures

2.1 Microtomography experiment

The material used was an Al-Si-Cu die cast aluminium alloy (ADC12, Japan Industrial Standard). ADC12 has a chemical composition range of 9.6 to 12.0 Si, 1.5 to 3.5 Cu, < 1.3 Fe, < 1.0 Zn, < 0.3 Mn, < 0.3 Mg, < 0.3 Ti, < 0.2 Pb, < 0.2 Sn and balance Al in mass %. A rectangular cylinder specimen, 0.6 × 0.6 mm in cross-section and 10 mm in length, was sampled from a die-cast automotive component, so that the casting surface was preserved as one of the four specimen side surfaces. No heat treatment was applied after casting. The specimen was exposed at 773 K for 0 to 92520 sec, with readings every second and periodic observation of blister formation and growth behaviour.

A high-resolution projection-type microtomography experiment was performed using the undulator beamline BL47XU of the SPring-8 facility. A monochromatic X-ray beam with X-ray energy of 20 keV, tuned by a liquid nitrogen-cooled Si (111) double crystal monochromator, was used. The specimen was positioned approximately 47 m from the X-ray source. The image detector, consisting of a cooled 4000 × 2624 element CCD camera used in 2 × 2 binning mode, a Ce doped single crystal Lu_2SiO_5 scintillator, and an optical lens (× 20), was positioned 20 mm behind the specimen, thereby making the imaging system sensitive to phase modulation. In total, 1500 projection radiographs, scanning 180 degrees, were obtained, with a rotational step of 0.12 degrees. The entire cross-section of the specimen and a region about 655 μm high were captured on the CCD camera. Tomographic images were reconstructed from a series of projections based on the convolution backprojection algorithm. The size of an isotropic voxel in the reconstructed slices was 0.503 μm, by which spatial resolution of about 1 μm is realized. The grey value in each set of reconstructed images was calibrated such that the linear absorption coefficient of -9 to 47 cm^{-1} fell within an 8-bit gray scale range between 0 and 255.

2.2 Image analysis

To estimate the volume of each micro pore/blister with sub-voxel accuracy, pentagonal facetted iso-intensity surfaces were computed from the volumetric data set using the conventional Marching Cubes algorithm [12]. To suppress inaccuracies originating from image noise, only micro pores over 23.168 voxels in volume were counted in the quantitative analysis. The threshold value for obtaining binary images was set at 64 and 140 for pores/blisters and particles, respectively. The volume, surface area and gravity centre of all the pores/blisters were measured in 3D images. Similar data for the particles were used for the subsequent particle tracking.

A two-frame particle tracking technique, called the matching parameter method, was employed to match identical particles in the series of tomographic images. The

details of the technique are available elsewhere [13]. In addition, a cluster matching technique, called the modified spring technique, was employed for tracking agglomerated particles with almost 100 % accuracy [13]. The coefficients α, β and γ, and the search range in the matching probability parameter, all as in Kobayashi et al. [13], were determined to be 0.9, 0.05, 0.05 and 100 μm, respectively, after systematically searching for the optimum condition in a preliminary trial in which a success ratio close to 100 % was achieved.

Tetrahedrons with vertices occupied by successfully tracked particles were generated by the Delaunay tessellation technique [14]. All the strain components were calculated from the deformation of the tetrahedron, assuming a linear displacement field within it.

2.3 3D image-based numerical simulation

First, polygonal surface meshes of pores and the blister nucleus were extracted from the tomographic volume shown in Fig. 1 (a), captured at the thermal exposure time of 5616 sec, by tracing iso-grey value surfaces. The numerical simulation predicted the state at 17640 sec with this model. It is physically impossible to completely reflect in meshing the detailed microstructural features visible in the high-resolution microtomography image, and then perform a finite element simulation, due to the enormous computation time required. Thus, to achieve a dramatic reduction in model size, only every 7th voxel of the original tomographic volume was taken into account, and only pores larger than 10 μm in diameter were modelled. The vertex positions of the polygonal mesh were determined through trilinear interpolation of gray values in the surrounding voxels. The polygonal model was exported as an STL file, enabling mesh generation for visco-plastic finite element analysis using PATRAN for format conversion. 4-noded tetrahedral elements were employed, with some loss of accuracy, in order to facilitate the conversion. The mesh model consisted of a uniform aluminium alloy embedded with a realistic complicated blister nucleus and 189 hydrogen micro

pores modelled as spheres of equal volume for the sake of further reduction in model size. The initial number of surface triangles was 16520, and the number of meshes and nodes in the final finite element model was 1119024 and 583806, respectively.

A commercial finite element analysis program, ANSYS, was used for the simulation. The necessary input parameters for the properties of the aluminium matrix were obtained from the experimental stress-strain curve of a corresponding bulk material. A generalized Garofalo creep model was employed to analyze the steady-state creep property of the aluminium alloy. Internal gas pressure in the pre-existing pores was calculated either with Eq. 1 or by incorporating the reported gas content in a die cast ADC12 alloy (24.6 cc / 100 g S.T.P for N_2, and 10.7 cc / 100 g S.T.P for CO_2) 7. Since the solubility of N_2 and CO_2 gases in aluminium alloys is very low, the internal gas pressure values for the pre-existing pores were simply calculated based on the ideal gas law.

3. Blister growth behaviour

3.1 The blister nucleus and its growth

In the in-situ observation of blister formation and growth behaviour, the largest pre-existing pore in the field of view gradually transformed into a blister. The blister nucleus and its change during the high-temperature exposure are shown in Fig. 2. Extracted 3D blister nucleus images are shown in Fig. 2, together with their corresponding two-dimensional images on identical virtual cross-sections. The results of the quantitative image analysis are shown in Fig. 3, where the size of the blister nucleus is expressed as that of the largest pore. The blister nucleus initially exhibited a complex shape (Fig. 2 (a)), and then became almost spherical by the thermal exposure time of 562 sec (Fig. 2 (c)). The size of the blister nucleus, expressed as an equivalent diameter for a sphere of equal volume, varied monotonically from 99 to 254 μm, over the thermal exposure of 70920 sec. It is reasonable to assume that the blister nucleus is filled with

high pressure gas, and that its growth and change in shape are attributable to the creep deformation of the surrounding aluminium due to this high gas pressure. In addition, a pointed projection began to form around the top of the blister nucleus after 562 sec (Fig. 2 (c) to (e)), gradually extending parallel to the casting surface. On the bottom side of the blister nucleus, a relatively coarse pore, approximately 40 μm away at the exposure time of 5616 sec, grew toward the blister nucleus (Fig. 4). Fig. 5 shows an image of the blister at 92520 sec. The blister nucleus has extensively coalesced with neighboring coarse pores to form a slender, conglomerated blister, parallel to the casting surface, reaching a millimeter in length in the longitudinal direction.

3.2 Surface elevation

Surface elevation was also observed after the thermal exposure time of 5616 sec (Fig. 2 (c) to (e)), and the blister formation was macroscopically observable at the stage shown in Fig. 5. The flow of the matrix material has been rendered in 3D, in Fig. 6, by tracking particles between 5616 and 17640 sec. The vectors represent the displacement of individual particles, projected onto the *x*-*z* plane. Extensive deformation toward the casting surface is observed, together with expansion of the largest pore, which spreads across a wide area of about 5 times the largest pore size parallel to, and 3 times the largest pore size perpendicular to, the casting surface. The particle displacement is much larger in the region between the blister nucleus and the casting surface than in the other regions. This is of course due to the lower constraint in the sub-surface region due to the existence of free surface. The experimentally measured strain distributions (all three normal strains and the equivalent strain) are shown in Fig. 7. It is obvious that the expansion of the blister nucleus generates tension in the circumferential direction, and compression in the radial direction, in the matrix aluminium around the blister nucleus; hence the formation of the large strain band, of about 30 % of the diameter of the blister nucleus, shown in Fig. 7 (d). Small patches of high strain are also scattered over the field of view.

3.3 Hydrogen precipitation

Upon closer inspection of Fig. 2 (c) to (e), it is observed that microscopic and almost spherical pores are precipitated throughout the field of view, with a relatively homogeneous spatial distribution. Fig. 3 shows the total volume fraction, number density and mean equivalent diameter of the micro pores. The number density rapidly increased to approximately 30 times the initial value at 1000 sec, and then began to decrease, while the total volume fraction increased monotonically. Considerable micro pore formation is also confirmed in Fig. 8, in which all the pores observed in the field of view are rendered. Since hydrogen is the only gas with measurable solubility in aluminium and its alloys [8], it is reasonable to assume that such micro pores are filled with hydrogen. It has been confirmed that the growth behaviour of such hydrogen micro pores at high temperatures is dominated by Ostwald ripening [15]. The corresponding continuous growth of relatively coarse pores and annihilation of fine micro pores is observed in Fig. 8, in which the underlying aluminium matrix and second-phase particles are not displayed. Notably, a pore-depleted band is observed around the blister nucleus, as is clearly shown in the virtual cross-sections captured at 5616 and 17640 sec (Fig. 2 (d) and (e)); and it is interesting to note that the width of the pore-depleted band corresponds well to that of the large strain band shown in Fig. 7 (d). It may therefore be inferred that micro pore formation was disturbed due to the existence of the compressive strain caused by the radial expansion of the blister nucleus.

4. Assessment of blister formation and growth mechanisms

4.1 Determination of internal gas species and pressure

As noted above, it is reasonable to assume that micro pores precipitated during the high-temperature exposure are filled with hydrogen, however the composition of the internal gas in the pre-existing pores and the blister nucleus is unknown and

inaccessible to measurement due to these latter's small volume. Three different gas species were assumed in the case of the pre-existing pores and the blister nucleus (Fig. 9 (a) to (c)), while only hydrogen was assumed in the case of micro pores precipitated during the thermal exposure. Since the gas pressure is always in thermal equilibrium with the surface tension of a matrix metal in the case of the precipitated micro pores, the gas pressure value varies with the micro pore diameter according to Eq. 1. In Fig. 9 (a), hydrogen was assumed in the case of both the pre-existing pores and the blister nucleus. In this case, the pre-existing pores and the blister nucleus are assumed to be formed during solidification and/or subsequent cooling. The gas pressure in the pre-existing pores and the blister nucleus is also assumed to be in thermal equilibrium with the surface tension of a matrix metal, resulting in the gas pressure being dependent on diameter according to Eq. 1. The maximum gas pressure for the pre-existing pores, and the gas pressure for the blister nucleus, were calculated to be 0.45 and 0.024 MPa, respectively. In Fig. 9 (b), both the pre-existing pores and the blister nucleus were assumed to be filled with nitrogen. In this case, nitrogen gas inside the pre-existing pores and the blister nucleus was assumed to be entrapped during solidification. The gas pressure in the pre-existing pores and the blister nucleus is dependent on the amount of gas entrapped and the pressure applied to a solidifying alloy inside a die cavity, resulting in the gas pressure being independent of diameter. The gas pressure for both the pre-existing pores and the blister nucleus was calculated to be 5.7 MPa by dividing the assumed amount of nitrogen gas entrapped in the alloy by the total volume of the pre-existing pores and the blister nucleus, as quantified in the 3D images of Fig. 8. In Fig. 9 (c), carbon dioxide gas was added to the case of Fig. 9 (b), and the gas pressure was 8.2 MPa for both the pre-existing pores and the blister nucleus.

It is obvious that the gas pressure values assumed in Fig. 9 (a) and (b) were too low to generate creep deformation, whereas a certain amount of creep deformation was predicted in the case of Fig. 9 (c). The simulated amount of creep deformation around the blister nucleus was similar to the measured equivalent strain shown in Fig. 7.

Although it is reasonable to assume that gas content is significantly influenced by casting conditions, it can at least be concluded that the nucleus of a blister is filled with insoluble gas that has been entrapped during solidification, thereby causing gas pressure high enough to cause creep deformation of the aluminium matrix during high-temperature exposure.

4.2 Blister growth mechanisms

It has been seen in this study that the growth of the blister nucleus occurs due to creep deformation of the aluminium alloy around the blister nucleus, which is filled with high pressure insoluble gases. It was also observed, in Figs. 2, 4 and 5, that the almost spherical blister nucleus of roughly a few hundred micrometers in diameter showed increased growth after thermal exposure of 562 sec, owing to the mechanism of surrounding micro pores being absorbed into the blister nucleus. It is reasonable to assume that axial and equivalent strain values are not sufficient to evaluate the growth behaviour of surrounding pores, and that pore growth is ensured when local hydrostatic stress around the pore is tensile and reaches a certain level. Local variation in hydrostatic strain can be precisely observed in Fig. 10. Although the hydrostatic strain is exceedingly high in the large strain band shown in Figs. 7 (d) and 9 (c), the creep deformation around the blister nucleus is not uniform. The hydrostatic strain is highly compressive in the region between the blister nucleus and the casting surface, but compressive hydrostatic strain is also observed on the opposite side of the blister nucleus. On the other hand, the hydrostatic strain is highly tensile around the top of the blister nucleus, which has been extended through the formation of the pointed projection after 562 sec, as shown in Fig. 2 (c) to (e). There obviously appears to be a high hydrostatic strain stripe connecting pre-existing pores A, B and C, and the direction of the stripe is consistent with the growth direction of the blister nucleus shown in Fig. 5.

The interaction between the hydrogen micro pores and the blister, and between the

pre-existing pores, is shown in Fig. 11. The presence of the hydrogen micro pores in the vicinity of the blister nucleus induces the elevation of hydrostatic strain in between them, due to the very low internal gas pressure in the hydrogen micro pores, as shown in Fig. 11 (a). The high hydrostatic strain inevitably accelerates the initiation of secondary micro-voids in between, thereby promoting the extension of the blister nucleus as a result of coalescence with the hydrogen micro pores. It is also reasonable to assume that hydrogen solubility is increased under hydrostatic tension. It may therefore be inferred that the generation of local hydrostatic stress around the blister nucleus might exert an additional positive effect on blister formation.

Notably, there are also a number of pre-existing pores, as shown in Fig. 8 (a), which sometimes causes clustering. Strong interaction among the pre-existing pores, obviously observable in Fig. 11 (b), results in the elevation of hydrostatic strain in between them, due to the superposition of the strain fields around them. Therefore they are prone to form larger pores through the mechanism of the coalescence of neighbouring pre-existing pores.

4.3 Practical implications

It has been shown that a combined contribution of entrapped insoluble gases and hydrogen is essential for blister formation. It seems most likely that the internal pressure of the blister nucleus may rapidly decrease with the blister's expansion and coalescence with neighbouring hydrogen micro pores. It is therefore conjectured that the contribution of hydrogen precipitation becomes more crucial as the blister formation process progresses. Fig. 9 clearly suggests that there is a distinct threshold level in the internal gas pressure at which blister growth is initiated, and this threshold gas pressure is fundamentally dependent on the creep strength of aluminium alloys at a specific temperature. It may be inferred that blister formation can be reduced by reducing entrapped gas and/or hydrogen, and further that such formation may be especially minimized by the reduction of entrapped gas below a threshold value and/or the

augmentation of creep strength through the addition of alloying elements such as copper and silicon, which enhance deformation resistance at high temperatures.

It is well known that blistering is observed even in wrought aluminium alloys. Since no air entrapment occurs during the production process of wrought aluminium alloys, the aforementioned combined contribution of entrapped insoluble gases and hydrogen is inapplicable in this case. On the other hand, it has been reported that high-angle grain boundaries behave as hydrogen trap sites in aluminium alloys [16,17], and indeed, it has been determined by the present authors that the trap site occupancy value is high for grain boundaries, ranging from 0.677 to 0.992 in the case of an Al–5.5 mol % Mg alloy. In addition, it has been claimed that grain boundary-trapped hydrogen concentration may be associated with hydrogen embrittlement behaviour [18,19]. It can therefore be inferred that the blistering of wrought aluminium alloys may be attributable to intergranular fracture and the subsequent opening of fractured grain boundaries due to hydrogen accumulation, which does not necessarily require high internal gas pressure if the grain boundary is located in the vicinity of free surface.

5. Conclusion

The previously unobserved fundamental origins and growth behaviour of a blister in a die cast aluminium alloy were observed in-situ using the synchrotron X-ray microtomography technique. Image-based numerical simulation was also employed to obtain the internal gas pressure of the blister nucleus, which has hitherto been unknown and inaccessible to measurement. It has been revealed that gases entrapped during die casting, such as nitrogen and carbon dioxide, fill the blister nucleus. Remarkably high internal gas pressure leads to the expansion of the blister nucleus due to the creep deformation of the surrounding aluminium matrix. Hydrogen precipitation and micro pore growth occur at the same time as the growth of the blister nucleus, resulting in further expansion of the blister nucleus through its absorption of surrounding hydrogen

micro pores and pre-existing pores. Due to the anisotropic distribution of hydrostatic strain around the blister, the blister nucleus undergoes directional growth, essentially parallel to the casting surface, resulting in the formation of a blister that is typically extended along the casting surface.

Acknowledgements

The synchrotron radiation experiments were performed with the approval of JASRI through proposal numbers 2007B1078 and 2010A1299. The authors wish to thank Mr. Shunzo Aoyama, Mr. Shin Orii and Mr. Shoji Ueda, of Ahresty Corp., for providing the die cast materials. The support provided to HT by the Light Metal Educational Foundation is also gratefully acknowledged.

References

1. G.O. Verran, P.K. Mendesb, M.A. Rossic: J. Mater. Process Tech., 2006, 179, 190−195.

2. K. Yano, K. Hiramatsu, Y. Kuriyama, S. Nishido: Int. J. Automation Technology, 2008, 2, 259-265.

3. R.L. III Schuyler: Mater. Perform.: 1979, 18, 9-16.

4. S.K.Yen, I.B.Huang: Mater. Chem. Phys., 2003, 80, 662-666.

5. X.C. Ren, Q.J. Zhou, G.B. Shan, W.Y. Chu, J.X. Li, Y.J. Su, L.J. Qiao: Metall. Mater. Trans., 2008, 39A, 87-97.

6. T. Izumi, G. Itoh: Mater. Trans., 2011, 52, 130-134.

7. K. Tomita, H. Taniyama, M. Imamori, H. Iwamura: J. Japan Inst. Light Metals, 1981, 31, 186-194 (in Japanese).

8. D.E.J. Talbot: Inter. Metall. Rev., 1975, 20, 166-184.

9. J.G. Kaufman: ‘Properties of Aluminium Alloys, Ohio, ASM, 264; 1999.

10. D.E.J. Talbot, D.A. Granger: J. Inst. Metals, 1963–64, 92, 290-297.

11. Y. Baba: Proc. ICSMA, 1968, 9, 356.

12.W. E. Lorensen and H. E. Cline. Computer graphics (ACM) 1987; 21: 163-169.

13. M. Kobayashi, H. Toda, Y. Kawai, T. Ohgaki, K. Uesugi, D.S. Wilkinson, T. Kobayashi, Y. Aoki, M. Nakazawa: Acta Mater., 2008, 56, 2167-2181.

14. C.B. Barber, D.P. Dobkin, H.T. Huhdanpaa.: ACM Trans. Math. Softw., 1996, 22, 469-483.

15. H. Toda, T. Hidaka, M. Kobayashi, K. Uesugi, S. Takeuchi, K. Horikawa: Acta Mater., 2009, 57, 2277-2290.

16. J.R. Scully, G.A. Young Jr., S.W. Smith: Mater. Sci. Forum, 2000, 331-337, 1583-1600.

17. S.W. Smith, J.R. Scully: Metall. Mater. Trans. A, 2000, 31A, 179-193.

18. D. Tanguy, Th. Magnin: Proc. EUROMAT 2000, 2, 1213-1218.

19. R. Edwards, W. von Eichenauer: Proc. Royal Soc., 1962, 270A, 90-102.

Caption list

Fig. 1 (a) 3D-rendered image of the blister nucleus and micro pores (note that only these features have been extracted, while the underlying aluminium and second-phase particles are not shown), and (b) an image-based finite element model, based on the blister nucleus and relatively coarse pores shown in (a).

Fig. 2 Variations in identical virtual cross-sections during high-temperature exposure. Sequential images of the blister nucleus have been extracted and rendered in 3D.

Fig. 3 Variations in (a) the largest and mean pore diameters, d_{max} and d_{mean}, and (b) volume fraction, V_f, and number density, ρ_p, of micro pores, during high-temperature exposure. The largest and mean pore diameters are expressed as equivalent diameters for a sphere of equal volume.

Fig. 4 3D-perspective views of the blister nucleus and a neighboring relatively coarse pore, at (a) 5616 sec and (b) 17636 sec.

Fig. 5 (a) a virtual cross-section of the final state, and (b) an extracted blister perspective-rendered in 3D.

Fig. 6 Particle displacement vectors projected onto the *x*-*z* plane, during high-temperature exposure of 5616 to 17640 sec, obtained by the particle tracking technique.

Fig. 7 Contour maps of (a) ε_x, (b) ε_y, (c) ε_z and (d) ε_{eq} on a virtual cross-section, showing strain increments for high-temperature exposure from 5616 to 17640 sec. Pre-existing pores are shown in black, hydrogen micro pores in white.

Fig. 8 3D-perspective views of micro pores during high-temperature exposure: (a) as-cast condition; (b) heat-treated after 178 sec, (c) 562 sec, (d) 5616 sec and (e) 17640 sec.

Fig. 9 Contour maps of equivalent strain obtained by image-based numerical simulation. Pre-existing pores and the blister nucleus are shown in black, hydrogen micro pores in white. The internal gas of the pre-existing pores and

the blister nucleus was assumed as (a) H_2, (b) N_2 and (c) N_2 + CO_2, with internal gas pressure of (a) 0.4 at the maximum, (b) 5.7 and (c) 8.2 MPa, respectively.

Fig. 10 Contour map of hydrostatic strain, ε_m, obtained by image-based numerical simulation.

Fig. 11 Contour maps of hydrostatic strain, ε_m, obtained by image-based simulation, showing magnified views that illustrate the interaction between hydrogen micro pores and the blister, and between the pre-existing pores.

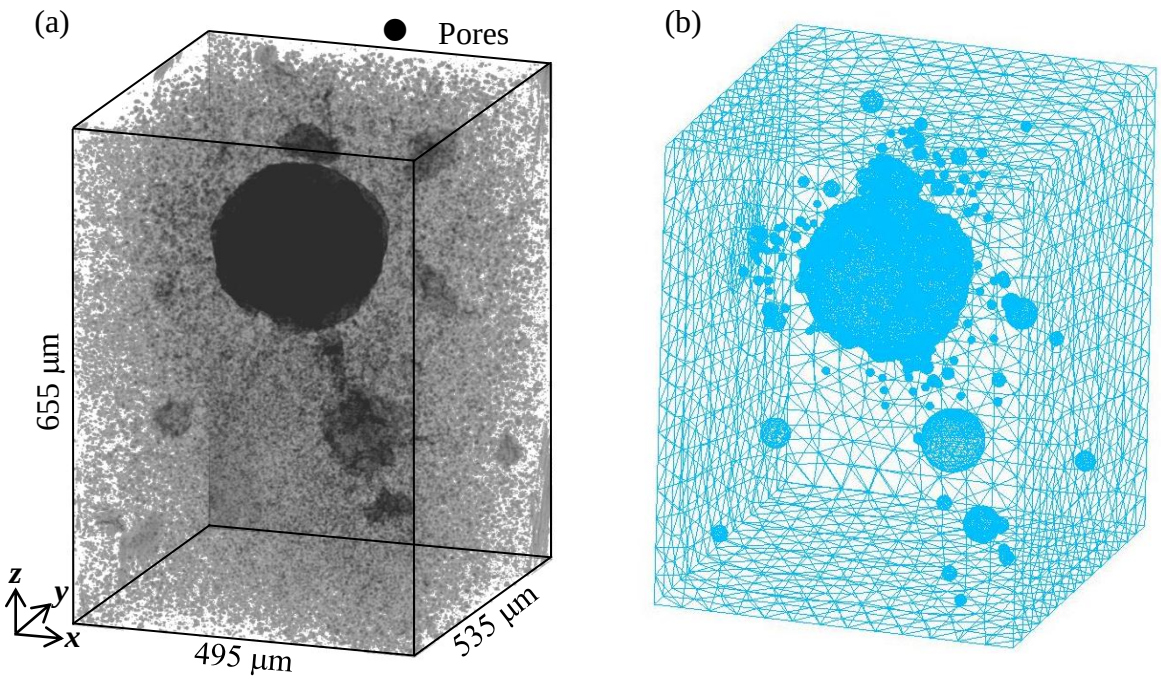

Fig. 1 (a) 3D-rendered image of the blister nucleus and micro pores (note that only these features have been extracted, while the underlying aluminum and second-phase particles are not shown), and (b) an image-based finite element model, based on the blister nucleus and relatively coarse pores shown in (a).

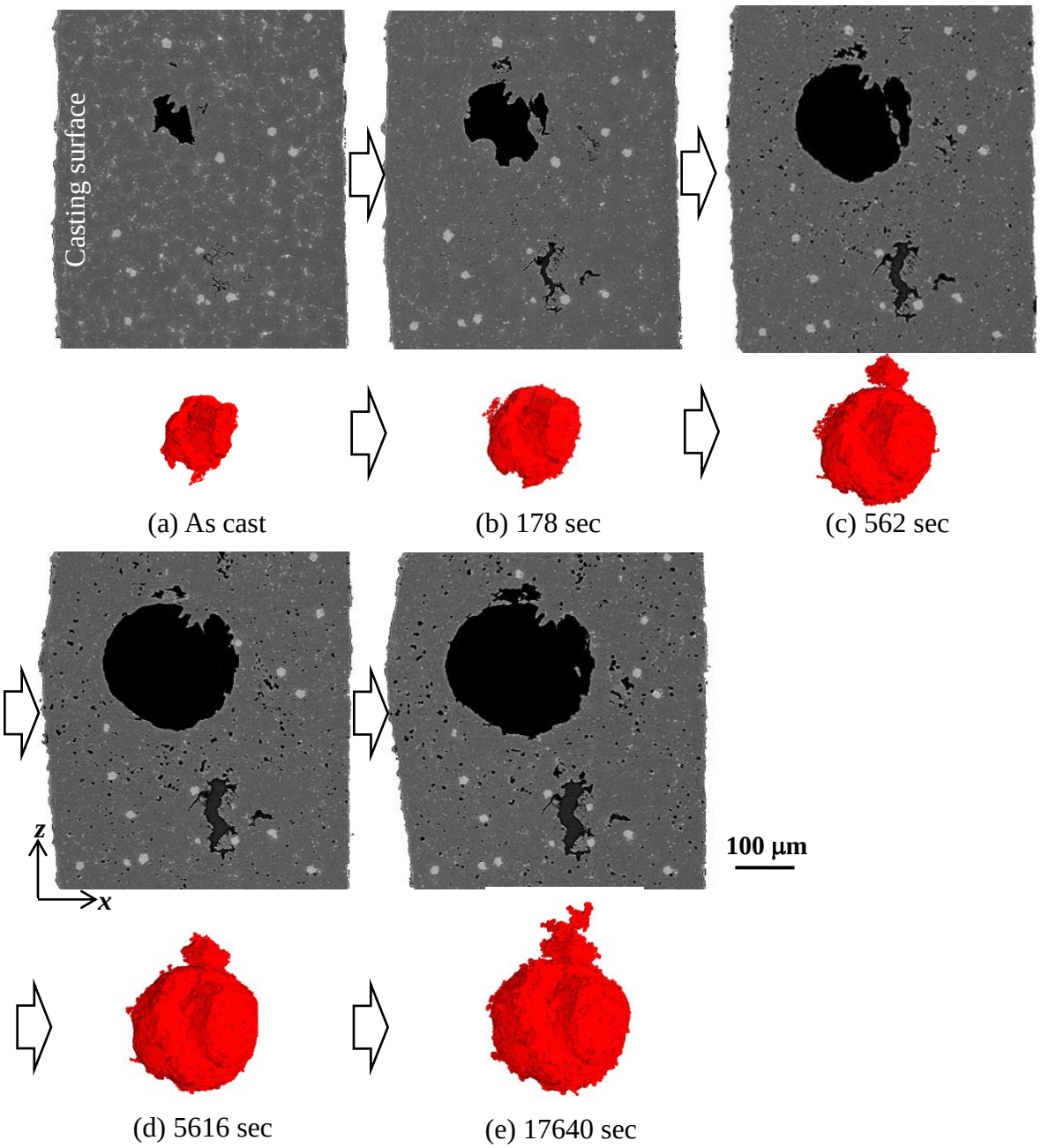

Fig. 2 Variations in identical virtual cross-sections during high-temperature exposure. Sequential images of the blister nucleus have been extracted and rendered in 3D.

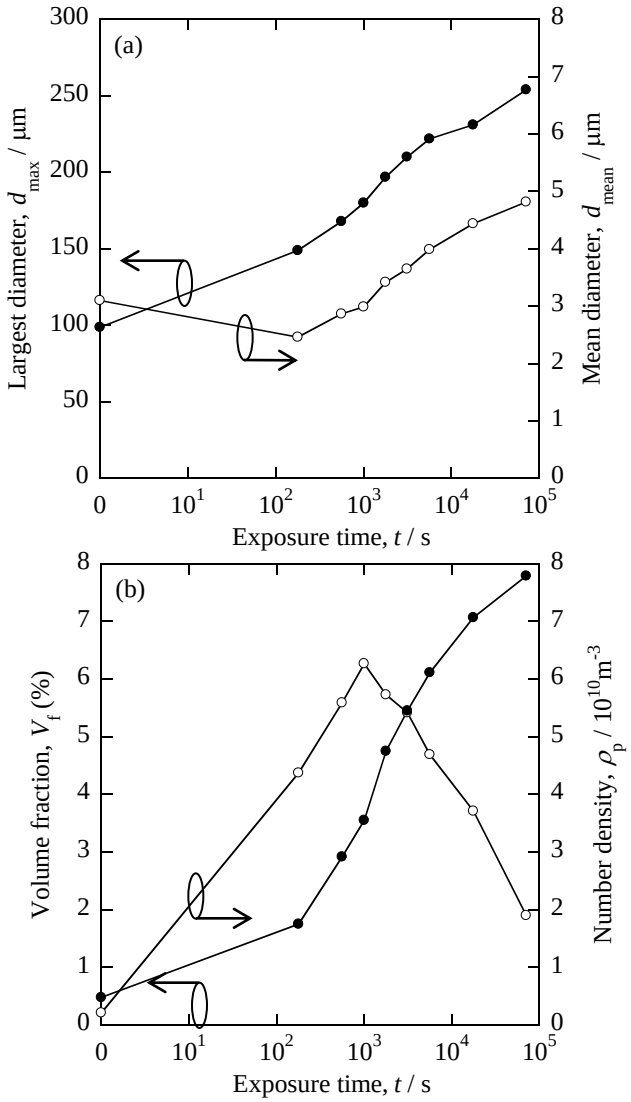

Fig. 3 Variations in (a) the largest and mean pore diameters, d_{max} and d_{mean}, and (b) volume fraction, V_f, and number density, ρ_p, of micro pores, during high-temperature exposure. The largest and mean pore diameters are expressed as equivalent diameters for a sphere of equal volume.

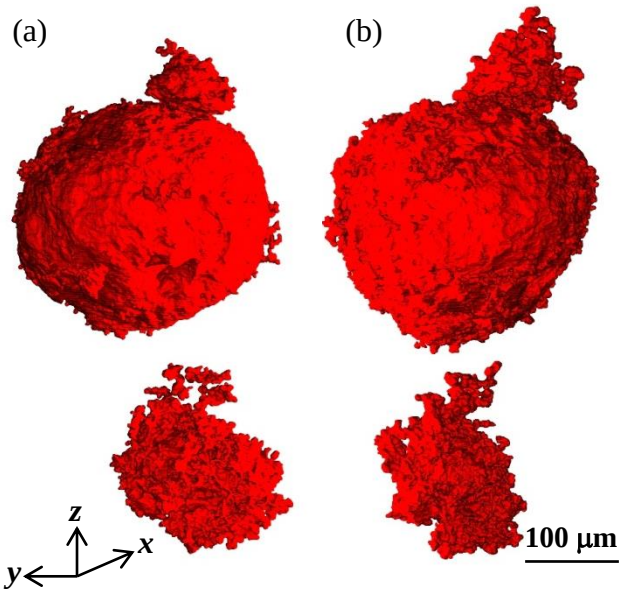

Fig. 4 3D-perspective views of the blister nucleus and a neighboring relatively coarse pore, at (a) 5616 sec and (b) 17636 sec.

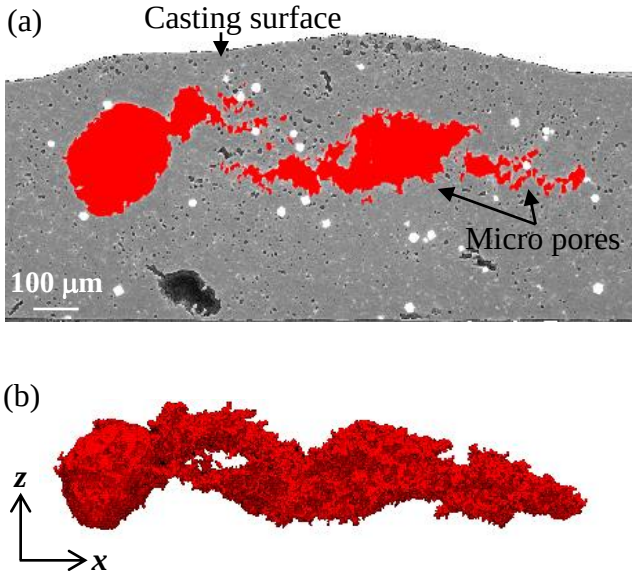

Fig. 5 (a) a virtual cross-section of the final state, and (b) an extracted blister perspective-rendered in 3D.

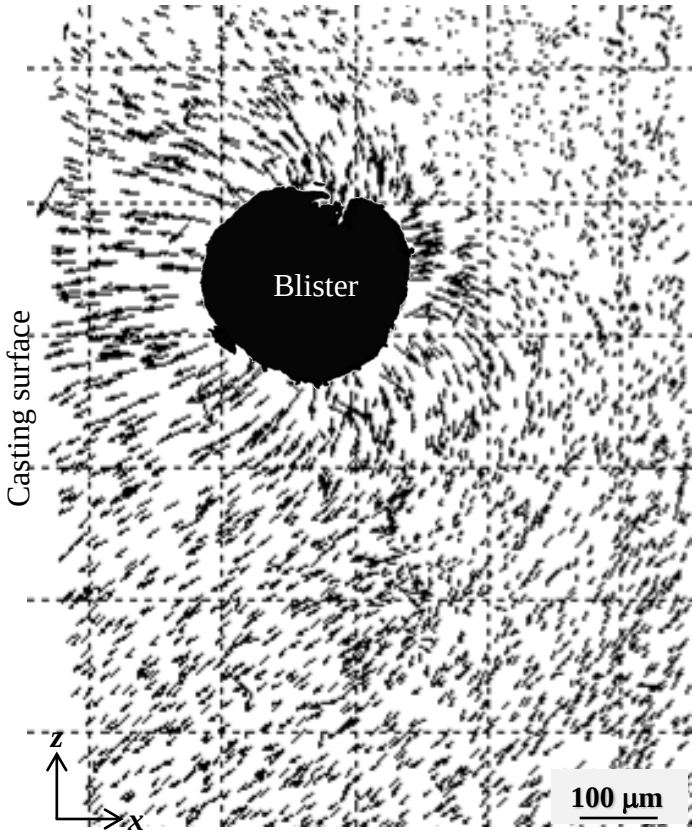

Fig. 6 Particle displacement vectors projected onto the x-z plane, during high-temperature exposure of 5616 to 17640 sec, obtained by the particle tracking technique.

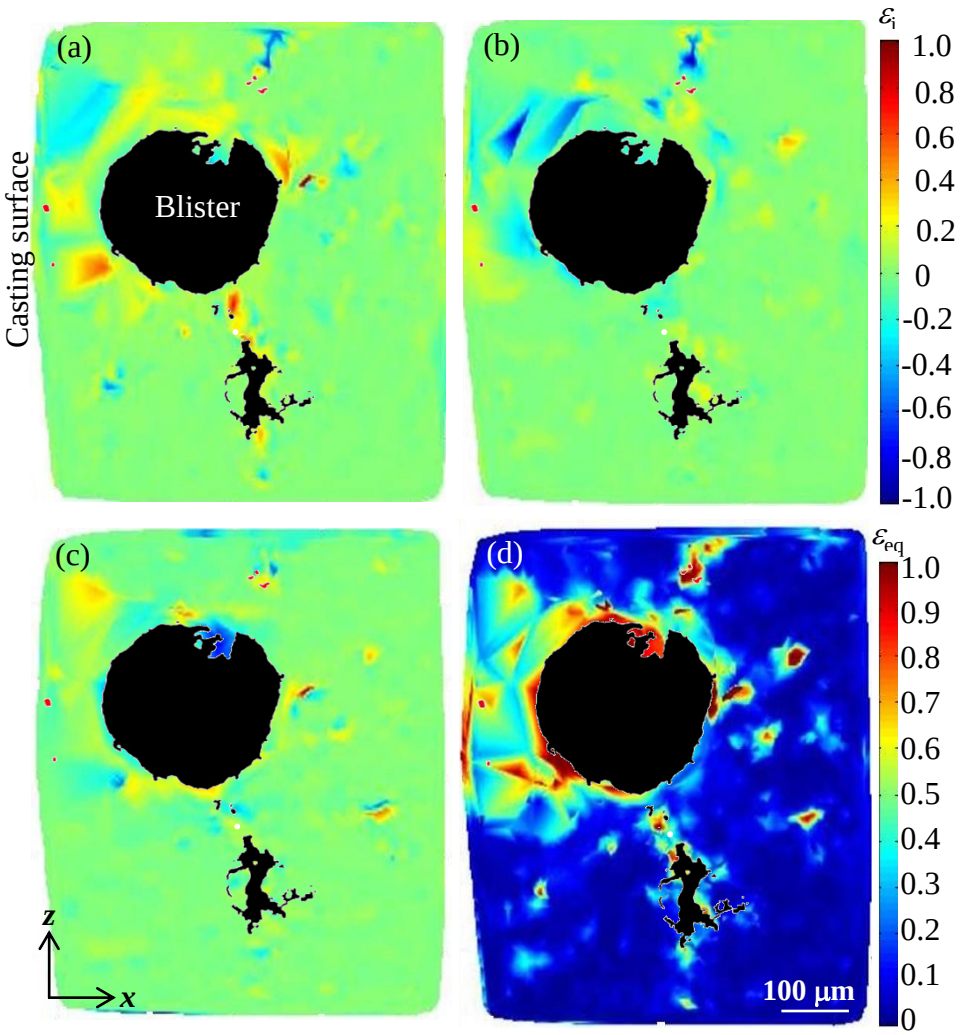

Fig. 7 Contour maps of (a) ε_x, (b) ε_y, (c) ε_z and (d) ε_{eq} on a virtual cross-section, showing strain increments for high-temperature exposure from 5616 to 17640 sec. Pre-existing pores are shown in black, hydrogen micro pores in white.

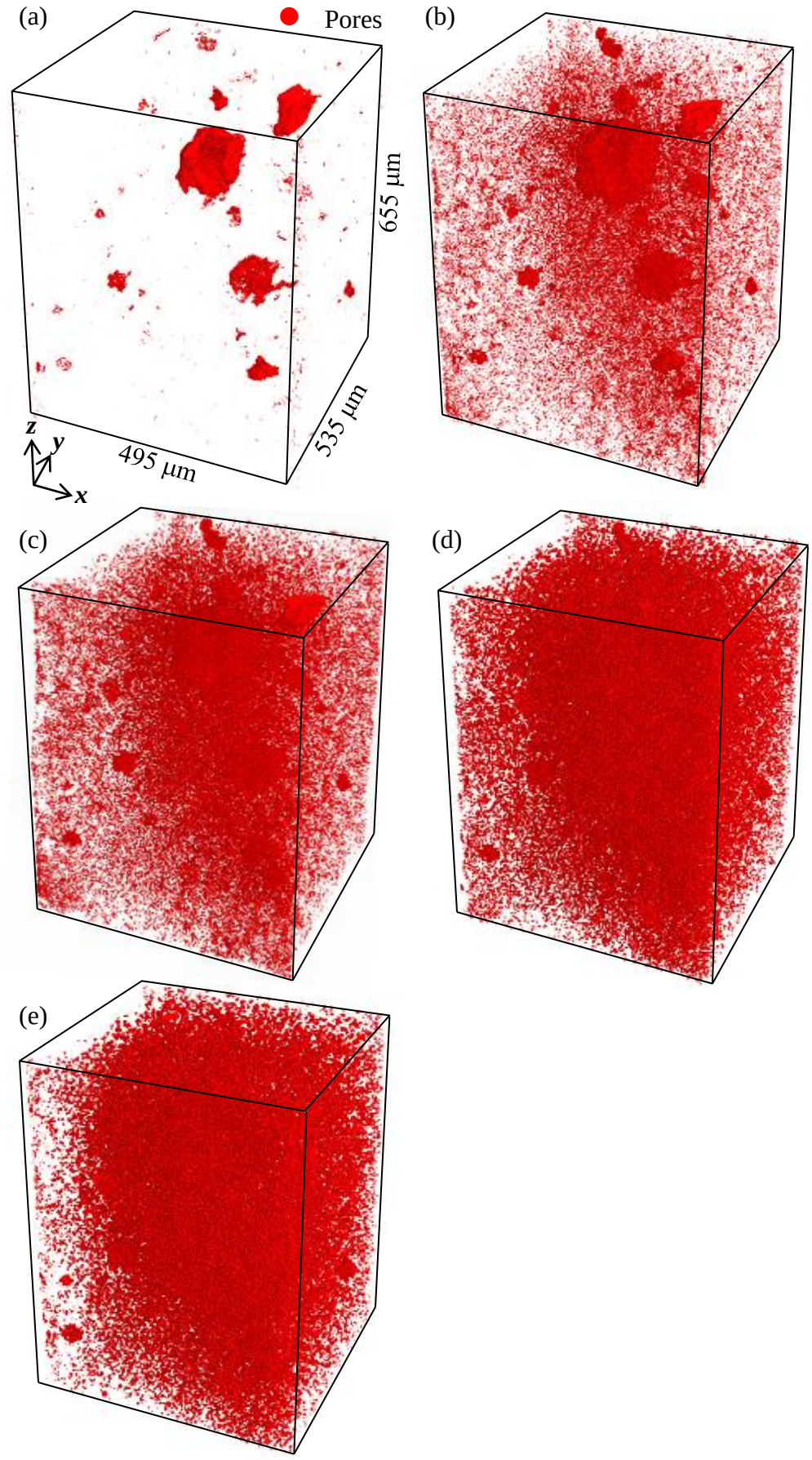

Fig. 8 3D-perspective views of micro pores during high-temperature exposure: (a) as-cast condition; (b) heat-treated after 178 sec, (c) 562 sec, (d) 5616 sec and (e) 17640 sec.

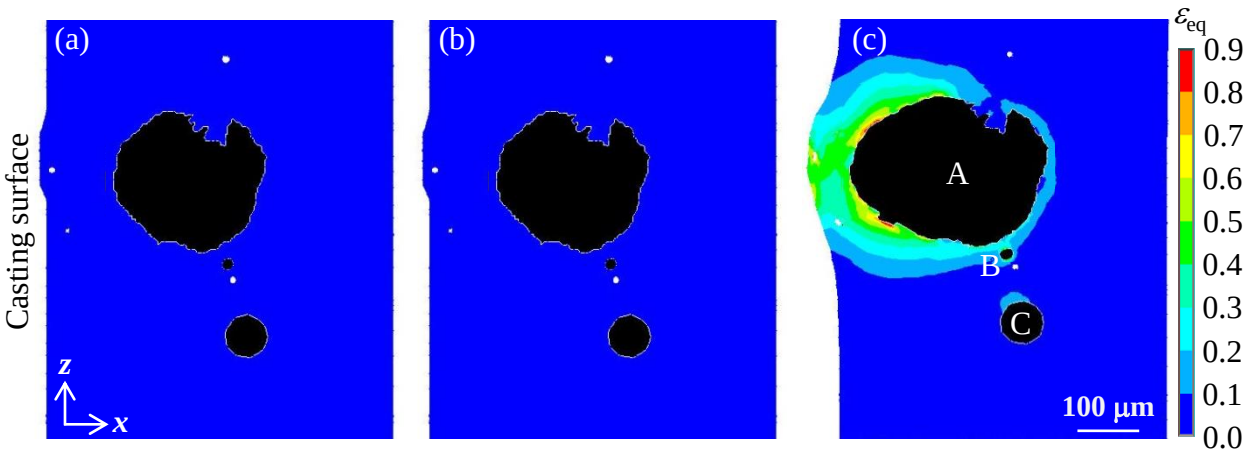

Fig. 9 Contour maps of equivalent strain obtained by image-based numerical simulation. Pre-existing pores and the blister nucleus are shown in black, hydrogen micro pores in white. The internal gas of the pre-existing pores and the blister nucleus was assumed as (a) H_2, (b) N_2 and (c) N_2 + CO_2, with internal gas pressure of (a) 0.4 at the maximum, (b) 5.7 and (c) 8.2 MPa, respectively.

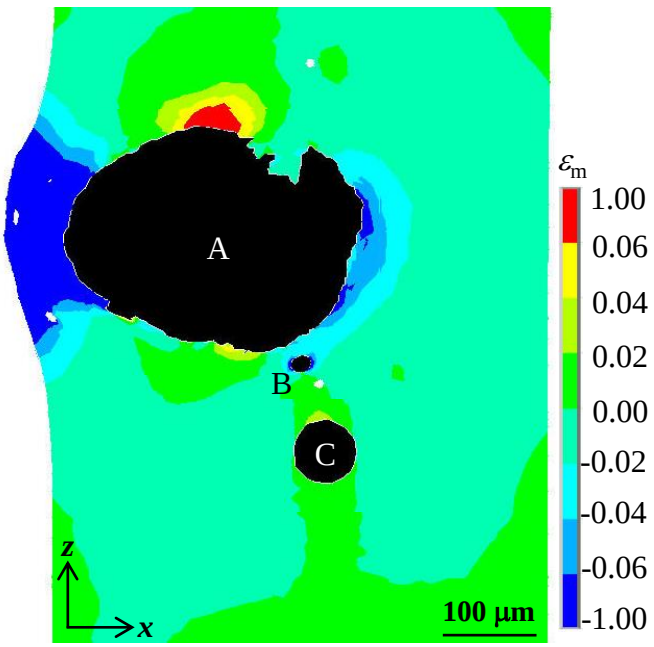

Fig. 10 Contour map of hydrostatic strain, ε_m, obtained by image-based numerical simulation.

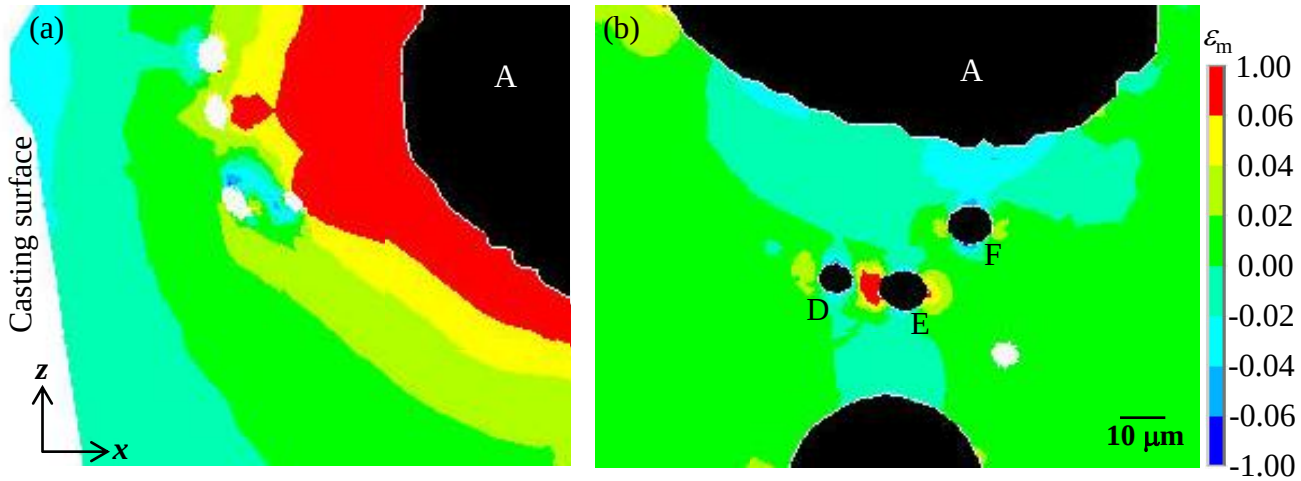

Fig. 11 Contour maps of hydrostatic strain, ε_m, obtained by image-based simulation, showing magnified views that illustrate the interaction between hydrogen micro pores and the blister, and between the pre-existing pores.